Int J Adv Manuf Technol (2015) 79:2067–2077
DOI 10.1007/s00170-015-6966-9

ORIGINAL ARTICLE

Online defect detection of Al alloy in arc welding based on feature extraction of arc spectroscopy signal

Zhifen Zhang · Elijah Kannatey-Asibu Jr · Shanben Chen · Yiming Huang · Yanling Xu

Received: 19 August 2014 / Accepted: 23 February 2015 / Published online: 14 March 2015

Abstract In this paper, a novel methodology for real-time nondestructive defect detection, particularly hydrogen-assisted porosity of an aluminum alloy welded using pulsed gas tungsten arc welding is presented based on the plasma spectroscopy signal of the welding arc. The emission lines of the hydrogen atom at 656.3 nm and argon atom at 641.63 nm were analyzed to extract multiple feature parameters, from which more sensitive features were then selected for monitoring by means of Fisher distance criteria. The threshold detection method based on the features selected from the spectrum was found to be feasible in detecting the welding defect, i.e., porosity in real-time. Furthermore, the established predicting model based on SVM-CV also successfully identified defect of porosity from normal welding with high accuracy.

Keywords Defect detection · Arc welding · Plasma spectra · Feature extraction · Fisher distance criteria · Data modeling

1 Introduction

Real-time monitoring of weld quality plays a key role in intelligent welding and quality control. Pulsed gas tungsten arc welding (GTAW) of aluminum alloys is widely used in the aerospace and automotive industries. The weld quality, in these situations, needs to be strictly consistent and free of defects, although process disturbances, such as changes of electrode position and joint geometry can result in variations in weld quality [1]. Both destructive and nondestructive evaluation techniques are used off-line to ensure that the quality of the weldment meets established standards, which obviously implies a significant cost in terms of productivity. To address this problem, several on-line weld monitoring techniques, such as vision [2–5], arc [6], acoustic emission [7–10], and temperature [11] sensing have been developed for online quality monitoring and control. In comparison, plasma spectroscopy has been shown to be a promising technique given its immunity to the strong electromagnetic interference and the robust analysis of different chemical species. Earlier work has shown its capability for detecting arc length in GTAW [12], measuring the concentrations of hydrogen in the welding arc [13, 14], evaluating seam quality during laser and TIG welding by estimating the electron temperature (T_e) of the plasma spectroscopy [15, 16]. However, estimation of T_e involves several processing stages such as peak detection and line identification, thus increasing the online computational time. In recent years, some feature selection methods such as principal component analysis have been applied to select the most useful information from the spectrum signal [16]. Besides, in our earlier research [17], some spectrum bands of interest (SOI) have been selected after line identification and careful analysis from which features extracted have successfully characterized and detected the defect of seam oxidation, among others. However, the porosity caused by hydrogen, which is one of the most common and damaging welding defects in GTAW welding of Al alloys, has seldom been reported in the literature.

In this paper, real-time quality monitoring of aluminum alloys in pulsed GTAW is presented based on the analysis of plasma spectroscopy signal. The porosity caused by hydrogen

Z. Zhang · S. Chen (✉) · Y. Huang · Y. Xu
Institute of Welding Engineering, Material Science and Engineering, Shanghai Jiao Tong University, Shanghai 200240, China
e-mail: zzf919@sjtu.edu.cn

E. Kannatey-Asibu Jr
Department of Mechanical Engineering, University of Michigan, Ann Arbor, MI 48109, USA

was artificially induced under controlled conditions during a butt welding experiment in order to simulate the welding defects. Six feature parameters were extracted from the selected area of spectrum bands to characterize the designed pulsed GTAW welding disturbance and seam defects. The proposed feature selection method was then utilized to select the parameters which are more sensitive to the welding defect and also enabled a reduction in feature dimensions. The validity of this technique was verified based on a series of experiments with different seam defects.

2 Experimental setup

The experiment system consists of three parts: the welding system, central control system, and signal acquisition systems, which can be found in Fig. 1; wherein the schematic of welding system is also displayed in Fig. 1a, including a TIG welding power source with OTC INVERTER ELESON 500P-type, CM-271 type wire feeder, and 99.99 % pure argon as the shielding gas. The central control system includes a host computer and control box from which the whole welding process can be controlled based on VC++ multithreading application, like arc on and off, movement of welding plate, welding current, wire feed speed, and so on. During the welding process, the workpiece moved while the torch was fixed so that the spectral sensor was stationary.

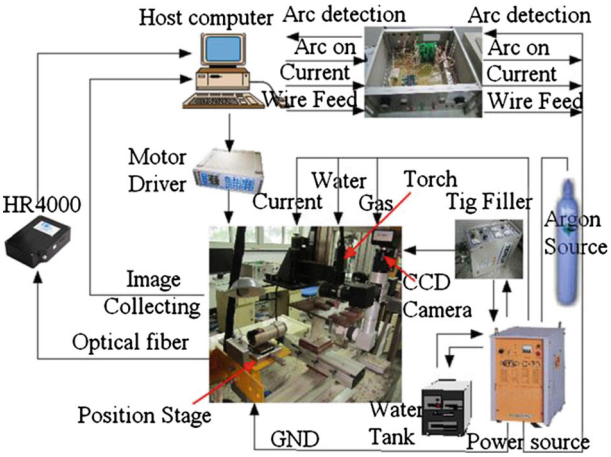

a) Schematic of welding system

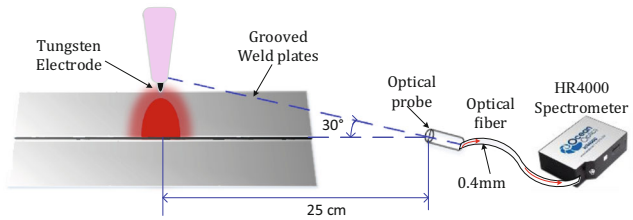

b) Signal acquisition system

Fig. 1 Experimental setup. **a** Schematic of welding system. **b** Signal acquisition system

Two kinds of welding signal were simultaneously collected, namely, the arc spectral and visual information of the weld pool, Fig. 1b. The vision monitoring system, which includes a CCD camera (DH-SV1420FM) and a filter-mirror, captures the weld pool image during the base-current period of every pulse. The spectral system consists of a 3648-pixel spectrometer (Ocean Optics HR4000), an optical fiber, and an optical probe. To ensure that the arc spectrum intensity was properly acquired, the optical probe was mounted on a two-dimensional positioning stage, approximately 25 cm from the electrode. The probe is also orthogonal to the torch axis and deviates 30° from the weld centerline. The spectrometer has a range of 185 to 1100 nm with a resolution of 0.2 nm. During the welding process, light emitted by the welding arc was detected by the spectrometer through the optical fiber and sampled with a period of 35 ms, resulting in a detection accuracy of 0.1 mm for the welded seam. The welding parameters have been shown in Table 1 as well as the welding plate condition. The composition of the base metal is shown in Table 2. Pulse frequency is one of the most important parameters for GTA welding process regarding the welding quality. In our experiment, the pulse frequency, 2 Hz, was determined using DOE and broadly used in most industry situation, which also matches the welding speed and welding current in order to acquire satisfied welding quality. Therefore, researching of the mechanism for typical welding defect, porosity in this paper, under standard welding processing is our priority task, which can give some guidance for our future research, such as using different pulse frequency, different size of welding plate, and so on.

One of the most significant reasons for hydrogen-assisted porosity occurring in welding process is the difference solubility of Al alloy for liquid and solidification condition. This kind of porosity greatly decreases the effective sectional area of welding seam, thus weakens the joint strength. Hence, minimizing the porosity can largely improve the strength of welding seam and decrease the possibility of crack and other developing inner defects and, finally, expand their service life. In this paper, a butt joint with a Y groove was used (Fig. 2).

Table 1 Normal welding parameters

Welding parameter	Value	Welding parameter	Value
Pulse frequency (Hz)	2	Welding speed (mm/s)	3
Peak current (A)	230	Wire feed speed (mm/s)	10
Base current (A)	50	Electrode diameter (mm)	3.2
Pulse duty ratio (%)	50	Welding wire diameter (mm)	1.6
Ar flow (L/min)	15	Plate size (mm)	300×50×4
Material type		Al-Mg Alloy (5A06)	

Table 2 Composition of base metal Al-Mg Alloy (5A06) (mass fraction %)

Al	Cu	Si	Mg
91.7~94.2	3.9~4.8	0.6~1.2	0.40~0.8
Mn	Zn	Ti	Ni
0.40~1.0	≤0.30	≤0.15	≤0.10

Defects were induced by drilling three holes of the same size at different positions in the plate by using the drill of diameter of 1 mm, and each was filled with a small amount of asphalt hydrocarbon, selected for its relatively high melting point. In addition, each workpiece surface was cleaned with a brush before welding. The objective of this research is to detect the impact that the designed disturbance will have on the arc spectrum signal, more specifically, features extracted from the signal. Since detection of seam porosity caused by hydrogen is the aim of this study, the analysis will focus on the spectrum of hydrogen element in the arc light to correlate the feature parameters extracted from the hydrogen spectrum line with the designed disturbance.

3 Results and discussion

The pulsed GTAW system used in this research has the AC frequency of 75 Hz and pulse frequency of 2 Hz. These frequency components are evident in the signal spectrum (Fig. 3). The spectral components for the base and peak current levels have different intensities. Hence, it is necessary to consider the pulse interference of the spectrum signal for effective defect detection in real-time.

3.1 Feature extraction

There are several sources of electromagnetic radiation associated with the welding process. These include the arc column, regions close to the electrodes, drops or droplets transported across the welding arc, the molten pool, the heated region of the base material around the molten pool, and the heated tip of the electrode [18, 19]. Thermal radiation is characterized by a continuous spectrum of radiation, mainly from the weld pool. Radiation characteristics of ions and atoms in the arc are discrete. The welding arc spectrum can be divided into different parts according to their wavelength, i.e., ultraviolet area between 200 and 400 nm, visible area between 400 and 750 nm, and infrared area from 750 to 1300 nm.

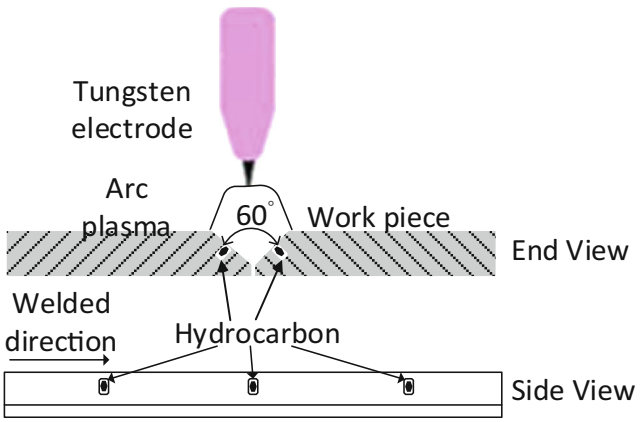

Fig. 2 Schematic of welding configuration showing disturbance locations

Figure 4 shows the spectrum of the signals acquired from both normal and defective welds, and the unit of spectrum intensity is a.u., meaning arbitrary unit. So is Fig. 5. It can be seen that most of the spectrum emission lines from metals, such as Al II, Al I, and Mg I were distributed in the ultraviolet and visible regions while the emission line of the argon atom is in the infrared zone. The selected spectrum area, i.e., the partially enlarged detail in Fig. 4 was analyzed for feature extraction considering the porosity defect. This part of the signal was selected based on research result of references [13, 14], where the concentration of hydrogen was successfully calculated by using the emission line of hydrogen and argon atoms. In this region, one strong emission line of the hydrogen atom with a wavelength of 656.28 nm was identified along with three nearby emission lines of the argon atom, from which the one at 641.63 nm with the lower intensity and close to the line of H I was selected for feature extraction, considering its smaller interference. It can also be seen that at the location where the designed disturbance and porosity occurs, the intensity of the H emission line is much higher than that for the normal welding condition. As a result, feature parameters will be extracted from the hydrogen emission line at 656.28 nm and argon atom at 641.63 nm.

3.1.1 Peak area based on trapezoidal rule

The area under some emission lines of specific wavelength can be an estimate of the spectrum energy of certain elements during the welding process. They can provide an indirect evaluation of the welding status. In this paper, the trapezoidal rule is used as the integration method for calculating the area under the selected emission lines. It generally has faster convergence than Simpson's rule for various classes of rougher functions and is also extremely accurate when periodic functions are integrated over their period. It is given by

$$\int_a^b f(x)dx \approx \frac{1}{2}\sum_{k=1}^{N}(x_{k+1}-x_k)(f(x_{k+1})+f(x_k)). \quad (1)$$

for $k=1, 2, \ldots, N$, where N is the number of samples in x.

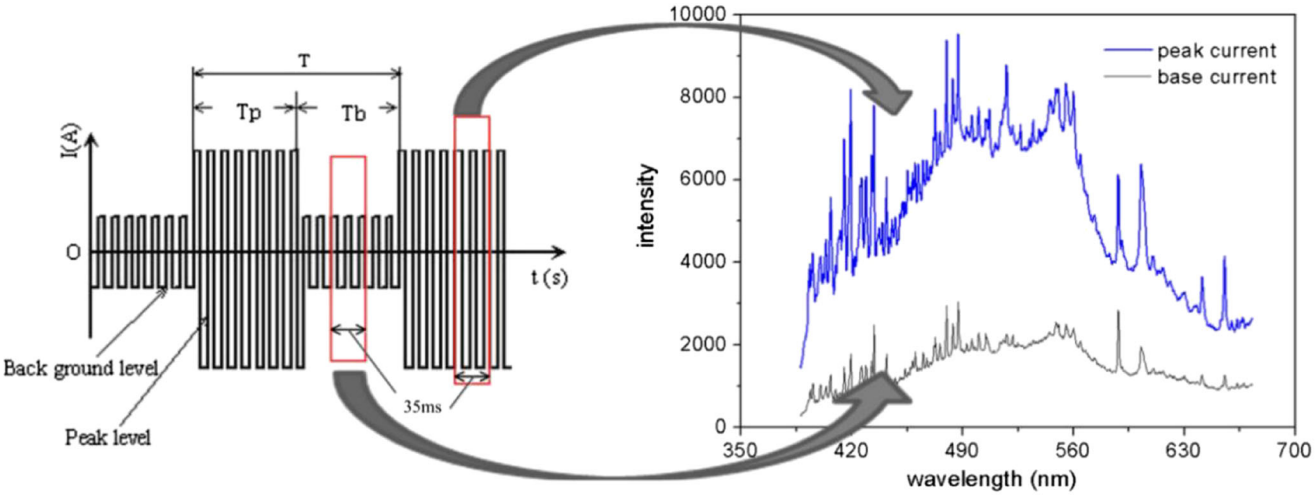

Fig. 3 Current and spectrum signals for pulsed GTAW

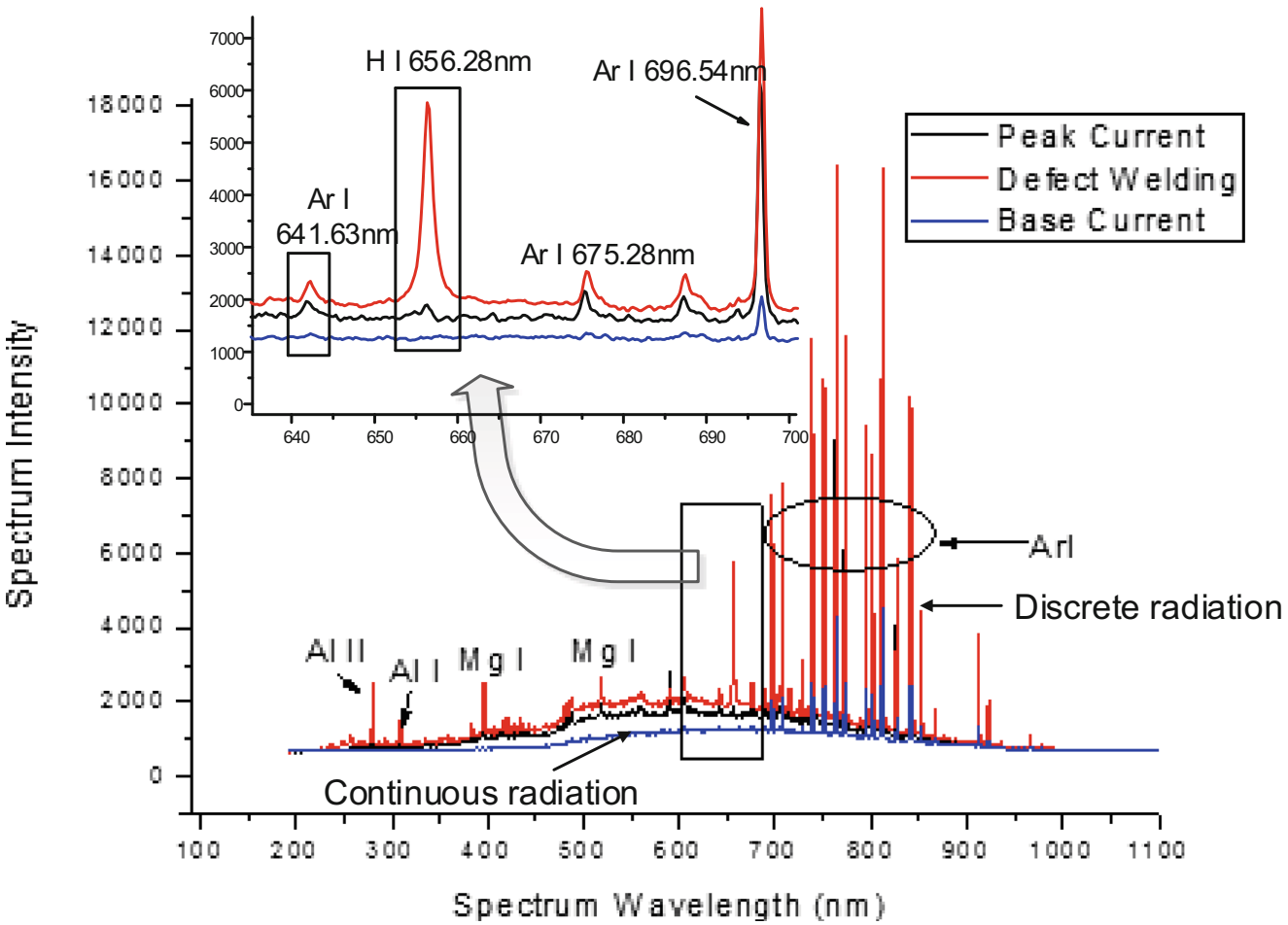

Fig. 4 Spectrum signals for different welding states

1) Peak area of hydrogen emission line

Figure 5 shows a schematic of the feature extraction process. The peak area of the hydrogen emission line at 656.28 nm was calculated using the trapezoidal rule as:

$$\text{Area H} = \int_{653.7526}^{659.7230} f(x)dx \tag{2}$$

where 653.7526 and 659.7230 are the starting and ending wavelengths, respectively.

2) Area ratio of H/Ar

The ratio between the peak areas of the H and Ar emission lines is another feature parameter extracted since it can eliminate some nonhydrogen interference, particularly heat accumulation, in terms of the detection of hydrogen-induced porosity. This is given by

$$\text{Area ratio} = \int_{653.7526}^{659.7230} f(x)dx \Big/ \int_{640.7020}^{644.0227} f(x)dx \tag{3}$$

where 640.7020 and 644.0227 nm are the start and end points, respectively, for the area calculation of the Ar emission line.

3.1.2 Peak intensity based on maximum rule

The intensity of the desired emission line is the most direct and significant parameter for detecting porosity. The traditional method of extracting the peak intensity usually involves several processing stages such as peak detection and line identification, before extracting the peak intensity. This increases the computation time. Besides, the position of the emission line usually has a certain degree of drifting due to hardware limitations. In this paper, the maximum rule is used to address these problems by extracting the maximum value from the selected spectrum region which contains the emission line of interest.

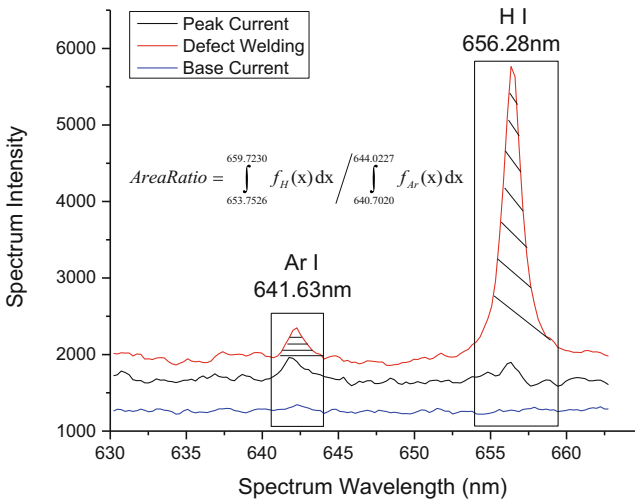

Fig. 5 Schematic of feature extraction

1) Peak intensity of hydrogen emission line

The intensity of the Hydrogen emission line at 656.28 nm was identified by choosing the maximum intensity in the range 653.7526 to 659.7230 nm.

$$\text{Peak H} = \max(f(653.7526)\sim f(659.7230)). \tag{4}$$

2) Peak intensity ratio of H/Ar

The intensity ratio was also calculated as a feature parameter.

$$\text{Peak ratio} = {}^{\text{Peak H}}/_{\text{Peak Ar}}. \tag{5}$$

where

$$\text{Peak Ar} = \max(f(640.7020)\sim f(644.0227)).$$

3.1.3 Variance

1) Variance of hydrogen emission line

The variance of the spectrum region discussed above around the peak was also used as a feature. This is statistically estimated as the deviation degree of the H emission line:

$$\text{Var H} = \frac{\sum_{i=1}^{n} \left(f_i - \overline{f_{\text{H}}}\right)^2}{n}. \tag{6}$$

2) Variance ratio of H/Ar

Likewise, the ratio between the variances of the H and Ar emission lines was extracted as:

$$\text{Var ratio} = {}^{\text{Var H}}/_{\text{Var Ar}}. \tag{7}$$

3.2 Feature selection

The Fisher criterion was used in this research. Feature selection can be grouped into supervised and unsupervised methods depending on whether or not class labels are considered. Supervised methods aim to choose the features that have the most discriminant information, measured by a certain criterion. The Fisher distance criterion is one of the supervised techniques [20]. It determines a subset of features, such that the distances between data points in different classes are maximized, while the distances between data points in the same class are minimized. Consider a feature space with C classes. Given n_i training samples (vectors) $\{x^i_1, x^i_{2,\ldots} x^i_n\}$ for each class i,(i=1,2,…C), the a priori probability of class i is estimated by $P_i = \frac{n_i}{\sum_{i=1}^{C} n_i}$. The class means are estimated by $\mu_i = \frac{1}{n_i}\sum_{j=1}^{n_i} x^i_j$, and the gross mean is estimated by $\mu = \sum_{i=1}^{C} P_i \mu_i$.

The sample covariance matrix S_i of class i is estimated by

$$S_i = \frac{1}{n_i}\sum_{j=1}^{n_i}\left(x^i_j - \mu_i\right)\left(x^i_j - \mu_i\right)^T. \tag{8}$$

The within-class scatter matrix and between-class scatter matrix are estimated by

$$S_w = \sum_{i=1}^{C} P_i S_i \tag{9}$$

and

$$S_b = \sum_{i=1}^{C} P_i (\mu_i - \mu)(\mu_i - \mu)^T \tag{10}$$

respectively. The kth feature is given by

$$\text{Fisher}(k) = \frac{S_b{}^{(k)}}{S_w{}^{(k)}} \tag{11}$$

In this paper, six features were selected, and their sensitivities then evaluated. Only two classes were considered (C=2), namely, normal welding and defective welding for which equal samples were calculated. Thus, P_i=0.5. The Fisher distances and variation of feature magnitudes during the welding process are shown in Fig. 6, wherein the unit for peak area is $(\text{a.u.})^2$ and the ratio feature has no unit., while the unit of peak intensity is a.u. as well as peak variance.

The results show that the highest Fisher distances occurred for the peak area ratio of H/Ar in Fig. 6b and peak intensity ratio of H/Ar in Fig. 6d with values of 3.01 and 2.96, respectively. The peak variance of hydrogen had the lowest value with 1.79. The higher the value of Fisher distance is, the feature parameter demonstrates more correlation with the welding defect, and thus, it has more sensitivity to designed defect. The feature selection method, here Fisher distance, helps reducing the dimension of feature space, more importantly; it is capable of evaluating their ability in terms of classifying defect welding from normal welding condition. In this case, the peak area ratio of H/Ar has the highest sensitivity to porosity and the best potential for classification.

As indicated earlier, the pulse interference has significant impact on the feature. It is quite obvious that the two features in Fig. 6e, f show the least pulse influence for normal welding regions due to the method used in calculating the ratio which is designed to eliminate most of the pulse interference. The amplified regions in Fig. 6b, e show more details about the pulse interference of both peak and base current period where weld defects occurred, especially the feature value of base current. Specifically, the value in Fig. 6e when there is a welding defect has almost the same value with that in normal welding, while in Fig. 6b it is higher than normal welding, which means that the feature in Fig. 6b has the better sensitivity and potential in monitoring the welding process, which also can be determined from the calculated Fisher distance.

3.3 Detection results based on STD threshold

Based on the selection criterion, the peak area ratio between hydrogen and argon, Fig. 5, was selected as the feature for monitoring the dynamic welding process. Figure 7 shows a plot of the feature value during normal welding using the welding conditions listed in Table 2 as well as the filtered curve obtained by wavelet transformation [17], with the db 4 function and 5 layer decomposition which enabled the pulse interference to be successfully eliminated. In Fig. 7, pictures of seam were also showed, including the front and back seam of the weld, clearly illustrating the region where there was lack of penetration due to reduced heat input. The feature had a higher amplitude in this region due to a higher radiation of hydrogen atoms in the welding arc spectrum. The feature gradually reduced in amplitude as the process became more stable.

A STD threshold method was also used to detect the weld quality by comparing the calculated feature parameter to its threshold as:

$$\begin{aligned} T^u_i &= m_i + \alpha \text{STD}_i \\ T^l_i &= m_i - \alpha\,\text{STD}_i \end{aligned} \tag{12}$$

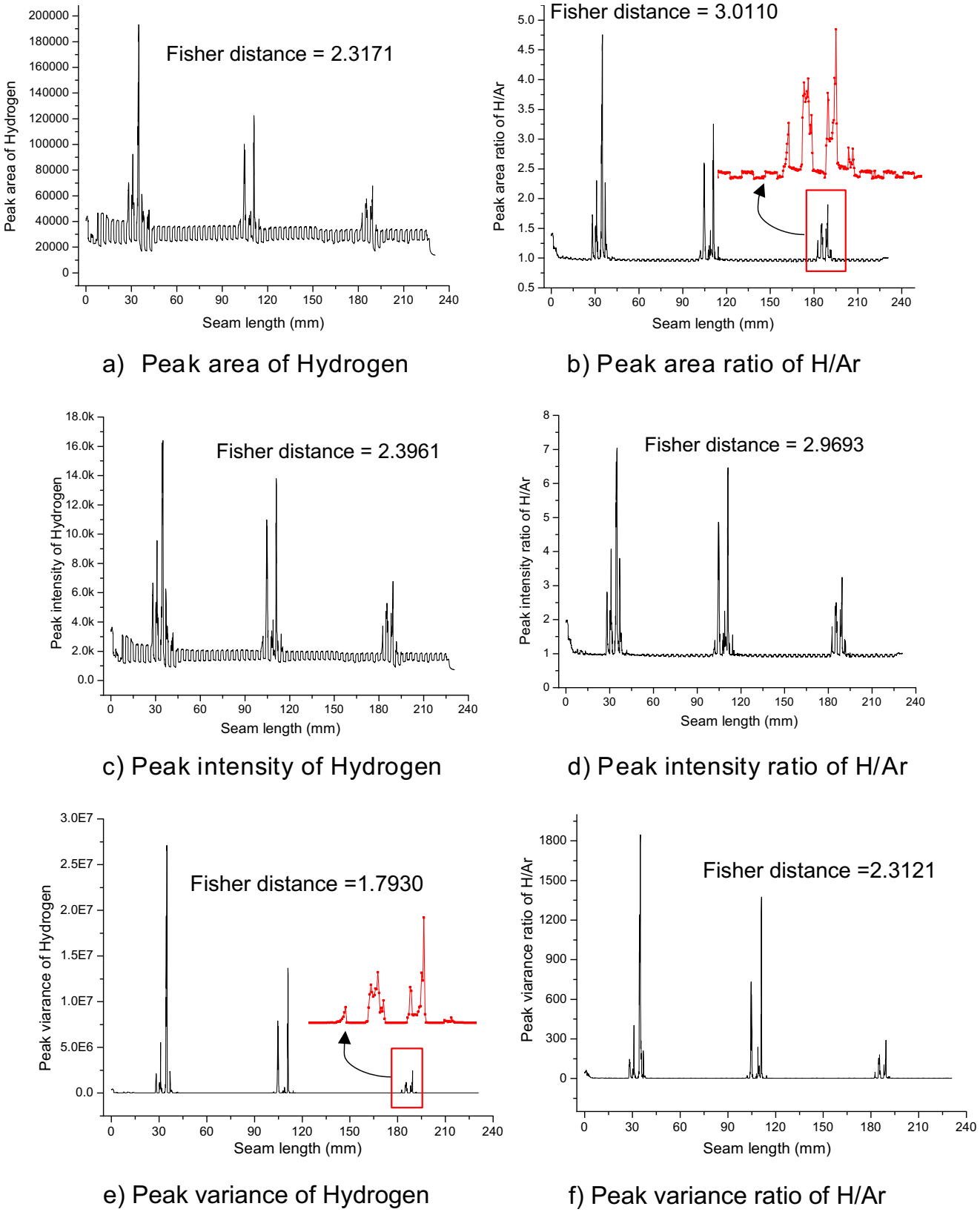

Fig. 6 Variation of feature magnitudes during the welding process. **a** Peak area of hydrogen. **b** Peak area ratio of H/Ar. **c** Peak intensity of hydrogen. **d** Peak intensity ratio of H/Ar. **e** Peak variance of hydrogen. **f** Peak variance ratio of H/Ar

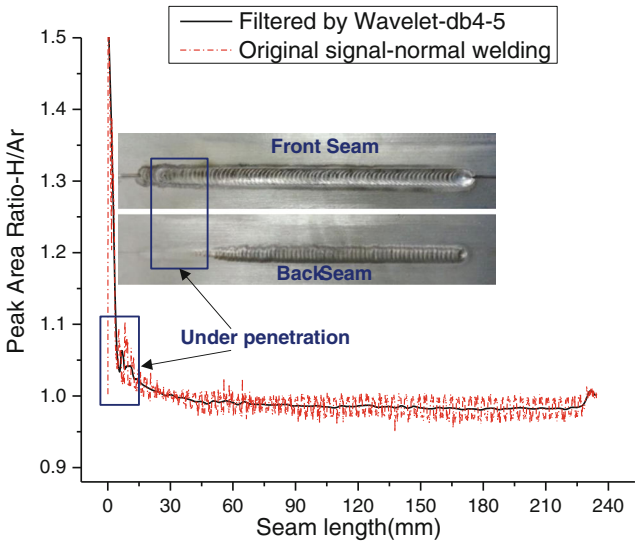

Fig. 7 Variation of the feature amplitude during normal seam welding

where T_i^u and T_i^l are the upper and lower thresholds, α is a positive number used to set the threshold width (typically 3), m_i is the mean value of the ith feature under normal welding conditions, and STD_i is the corresponding standard deviation. The welding defect was also quantitatively assessed by calculating its defect degree of exceeding the threshold, which is given by

$$\text{Def degree} = \frac{\left|\text{Fea}(x) - T_i^u\right|}{T_i^u} \times 100\% \tag{13}$$

where Fea(x) is the amplitude of the detection feature.

Some of the welded plates exhibited a certain amount of oxidation in three locations where some amount of hydrocarbon had been placed prior to welding. Porosity was observed at these locations.

At some of these locations, the porosity was severe enough to result in seam concavity. Defect of under penetration can be observed at the beginning of the weld because of the insufficient heat input, and the defect of burn-through can be seen at the end of the welding seam as a result of the combined effect of heat accumulation and preset hydrocarbon.

Figure 9 shows the defect detection result based on the feature parameter of AreaRatio. It also shows images of the weld pool for both defective and normal welding. It can be seen that the image obtained at the location where the induced defect is located shows contamination that includes a small amount of oxidation and the appearance of porosity. However, the weld pool image of normal welding did not show any such contamination.

The feature spike that results from defect formation depends on the type and severity of the defect, Fig. 8. For example, the severe defect marked in Fig. 9 with a magnitude of

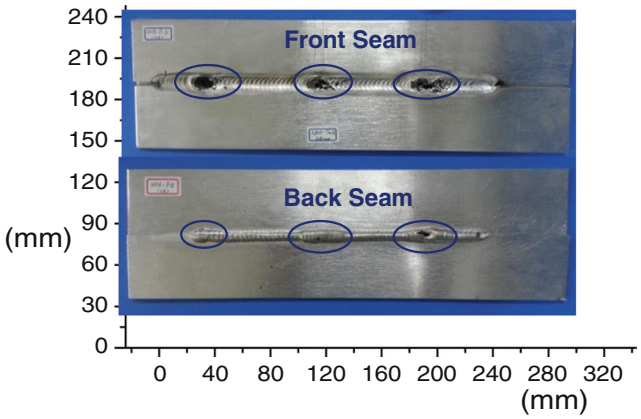

Fig. 8 Weld seam showing porosity at locations where hydrocarbon had been placed before welding

4.751 has a severity of 369.02 %, and the less severe defect has a magnitude of 1.126 and a severity of 11.15 % relative to the upper detection line. Moreover, the magnitude decreased as welding proceeded and welding heat accumulated for the workpieces even though the same amount of hydrocarbon was used at all three preselected defect locations. This could be due to evaporation of the hydrocarbon at the higher temperature, giving rise to a reduction in radiation of the hydrogen atom at 656.28 nm. This means sufficient melting and penetration of the weld pool will give the hydrogen more time to escape from it, reducing the possibility of generating hydrogen inside the weld bead. The results in Fig. 9 were in agreement with references [13, 14] indicating that the proposed method can successfully detect the hydrogen-assisted porosity. However, the defect of lack of penetration is not detectable by this method, given the results in Fig. 9. The reason for this result maybe that the features were extracted from the hydrogen element which is released when porosity occurs. Oxidation and concavity were also not detected by the proposed method, even though they had been successfully detected using features selected from spectrum bands of interest (SOI) from our early research [17]. Thus, the proposed method has the potential for detecting multiple defects provided the spectrum radiation of the appropriate chemical element is used.

3.4 Defect predict modeling based on SVM-CV

In the above section, various feature parameters have been extracted from spectrum signals and their sensitivity to the designed defect has been qualitatively analyzed based on Fisher distance. In this section, a classification model was established using developed support vector machine and cross validation (SVM-CV) method based on the selected features of spectrum signal to predict the defect of porosity. Figure 10 has plotted the flow chart of the proposed modeling architecture based on support vector machine and tenfold cross-

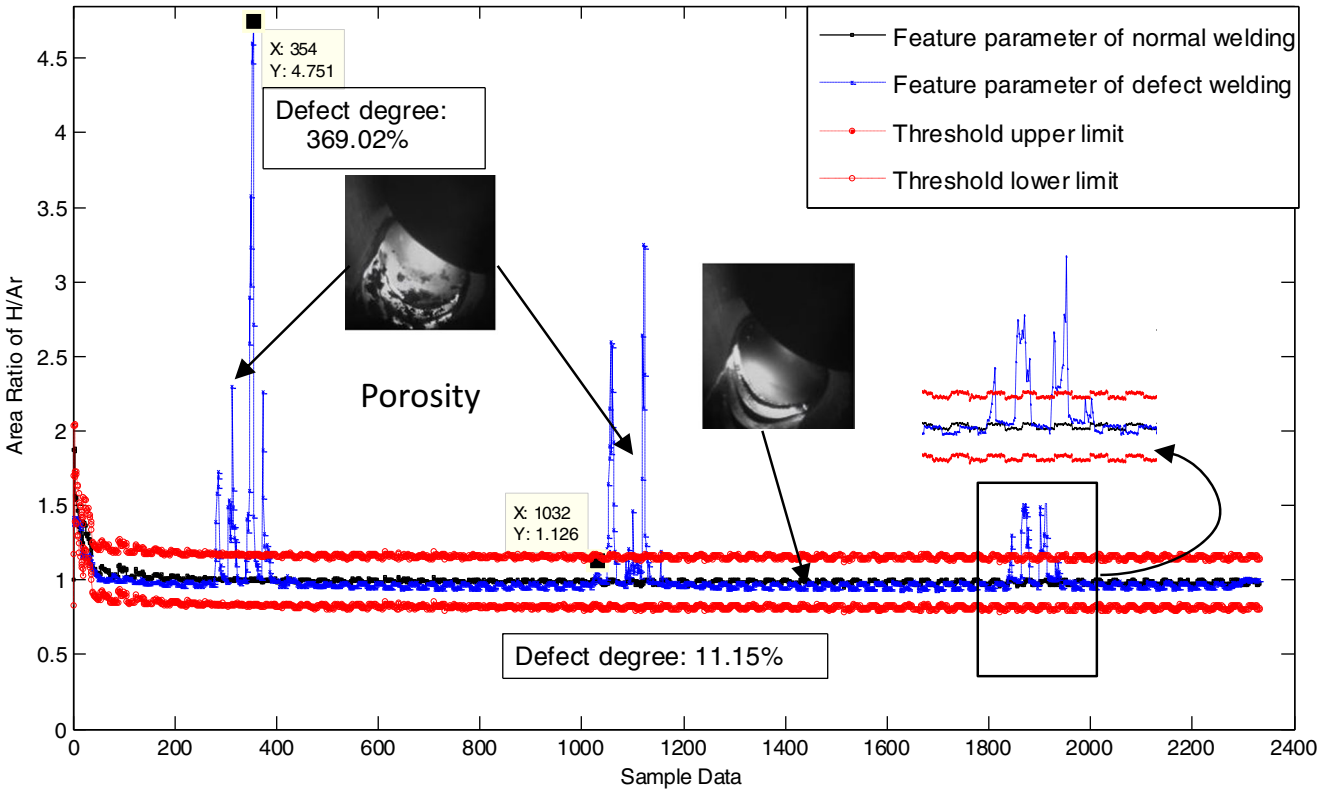

Fig. 9 Variation of area ratio of hydrogen to argon for a weld with porosity

validation, namely, SVM-CV classifier. After feature selection, two feature parameters with higher Fisher distance were chosen to establish the SVM-CV classifier. Eventually, the welding quality can be classified into two class using the predict model.

Recent research has indicated the considerable potential of SVM-based approaches for various intelligent classification issues since it is based on the notion that only the training samples that lie on the class boundaries are necessary for discrimination [21, 22]. Consequently, only a small amount of the training samples are actually required but also a high accuracy may be obtained. For multiclass and multifeature problems, it may be extended to allow for nonlinear decision surfaces. In this case, the input data are mapped into a high-dimensional space through some nonlinear mapping which has the effect of spreading the distribution of the data points

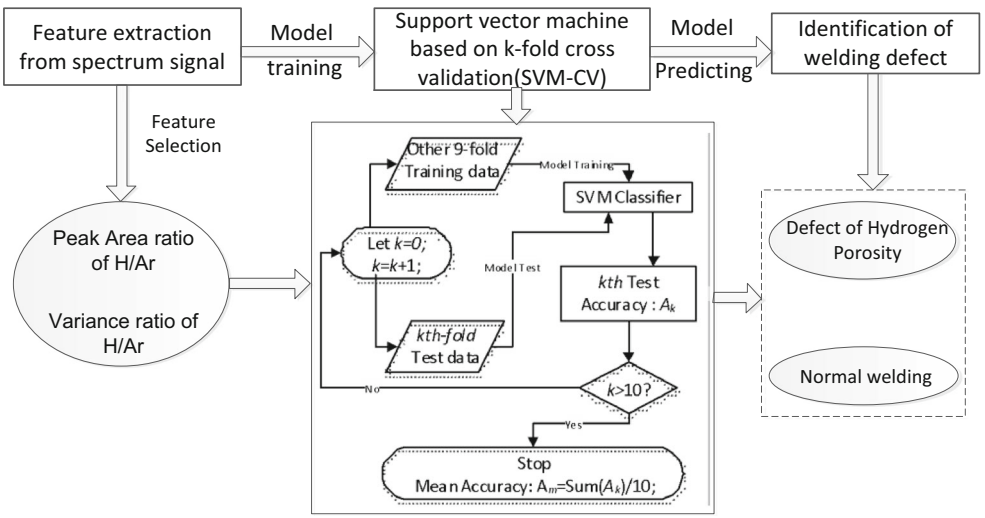

Fig. 10 Flow chart of predict modeling based on SVM-CV

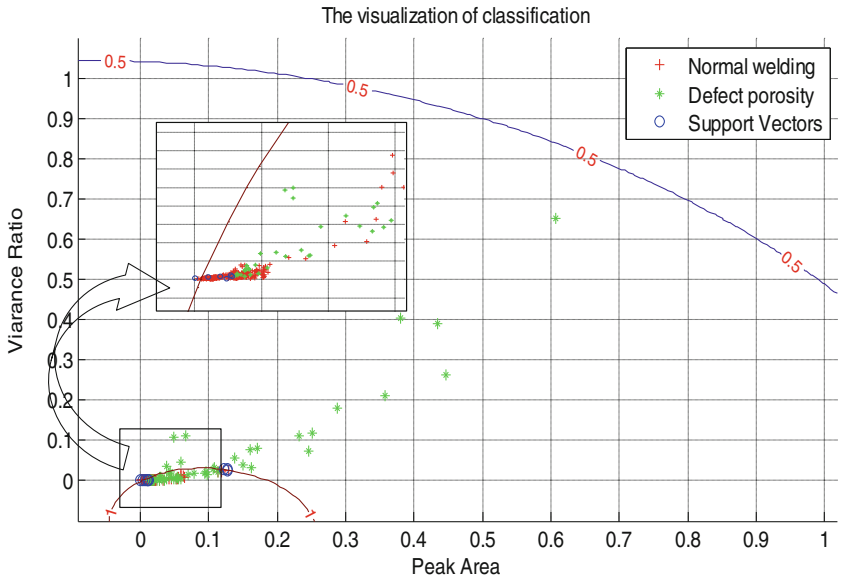

Fig. 11 Visualization of classification model based on SVM-CV

in a way that facilitates the fitting of a linear hyper lane. With this, the classification decision function becomes

$$f(x) = \mathrm{sgn}\left(\sum_{i=1}^{r} \alpha_i y_i k(x, x_i) + b\right) \tag{14}$$

where α_i, i=1,. . .,r are Lagrange multipliers and $k(x,x_i)$ is a kernel function. The radial basis function (RBF) is chosen as the kernel in this paper,

$$k(x, x_i) = e^{-\gamma \|(x, x_i)\|^2} \tag{15}$$

where γ and c is the parameter controlling the width of the Gaussian kernel. The accuracy with which a SVM may classify a data set is dependent on the magnitude of the parameters C and γ.

In this paper, cross-validation approach was applied to search the optimal value for these two parameters for the SVM model. Then, the classifier, i.e., SVM-CV was established based on cross-validation. In addition, ten-fold cross-validation is used and the mean accuracy for the established prediction model is achieved by calculating the mean value of each fold prediction. The k-fold cross-validation is widely used in the machine learning field in order to obtain a prediction error with more robustness and accuracy. The original sample is randomly partitioned into k equal size subsamples. Of the k subsamples, a single subsample is retained as the validation data for testing the model, and the remaining $k-1$ subsamples are used as training data. The cross-validation process is then repeated k times (the folds), with each of the k subsamples used exactly once as the validation data. The k results from the folds can then be averaged (or otherwise combined) to produce a single estimation. The advantage of this method is that all observations are used for both training and validation, and each observation is used for validation exactly once. In addition, the training and predicting of the SVM-CV was achieved through the combination of LIBSVM [23] and MATLAB.

The visualization of classification model can be found in Fig. 11, in which the lines with marker of 0.5 and 1 are the classification line and the support vectors are also marked in dot. Test result shows that this model has the detection accuracy of 100 %, which is quite high and showing the strengths of this proposed method. In addition, it also can be seen from Fig. 11 that the defect sample points distributed in larger space while the normal sample was more concentrated. From the enlarged rectangle, more information about the normal sample distribution can be clearly seen. There are some samples which are overlapping with each other, which are mainly from the phase of base current. Due to the lower heat input, the intensity of emission line from hydrogen and argon atom is decreased; moreover, the singularity of the porosity is less obvious than that of peak current. In addition, there is more data sample for defect welding condition than normal welding condition; hence, the established model has the character of unbalanced training data, which can be seen from Fig. 11 by the distribution of sample data. In future work, it is worth to use some other modeling technology to improve the robustness and stability of the whole system. Also, increasing more test methods would be of great importance to enhance the reliability of the proposed methodology.

4 Conclusions

A new method based on the analysis of spectral signal is presented for monitoring the quality of an Al alloy welded by pulsed GTAW. The following conclusions can be drawn from the results of the experiments:

1. The penetration of the weld bead has great impact on the emission line of the hydrogen atom at 656.28 nm and also on porosity.
2. The six features extracted from the hydrogen atom emission line at 656.28 nm and argon atom at 641.69 nm demonstrated different sensitivities to different defects during pulsed GTAW of an Al alloy.
3. The Fisher distance feature selection criterion was effective, resulting in the peak area ratio as the appropriate feature for monitoring the process.
4. Proposed predicting model based on SVM-CV has shown high accuracy and satisfied ability in detecting hydrogen porosity from normal welding.

Acknowledgments This work was supported by the National Natural Science Foundation of China under Grant No. 61374071 and No. 51405298 and the Shanghai Sciences & Technology Committee under Grant No. 11111100300.

References

1. Chen S-B, Wu J (2009) Intelligentized methodology for arc welding dynamical processes, vol 29. Springer, Berlin
2. Kovacevic R, Zhang Y (1997) Real-time image processing for monitoring of free weld pool surface. J Manuf Sci Eng 119(2):161–169
3. Zhang W, Liu Y, Wang X, Zhang Y (2012) Characterization of three-dimensional weld pool surface in GTAW. Weld J 91(7):195s–203s
4. Huang W, Kovacevic R (2012) Development of a real-time laser-based machine vision system to monitor and control welding processes. Int J Adv Manuf Technol 63(1–4):235–248
5. Ye Z, Fang G, Chen S, Zou JJ (2013) Passive vision based seam tracking system for pulse-MAG welding. Int J Adv Manuf Technol 67(9–12):1987–1996
6. Christner B (1998) Developing a GTAW penetration control system for the Titan IV program. Weld Met Fabr 66(3):33–38
7. Emel E, Kannatey-Asibu E (1988) Tool failure monitoring in turning by pattern recognition analysis of AE signals. J Eng Ind 110(2):137–145
8. Sun A, Kannatey-Asibu E Jr, Gartner M (1999) Sensor systems for real-time monitoring of laser weld quality. J Laser Appl 11(4):153–168
9. Sun A, Kannatey-Asibu E Jr, Gartner M (2002) Monitoring of laser weld penetration using sensor fusion. J Laser Appl 14(2):114–121
10. Kannatey-Asibu E Jr (2009) Principles of laser materials processing, vol 4. John Wiley & Sons, New York
11. Chen W, Chin B (1990) Monitoring joint penetration using infrared sensing techniques. Weld J 69(4):181s–185s
12. Li P, Zhang Y (2001) Robust sensing of arc length. Instrum Meas IEEE Trans 50(3):697–704
13. Shea JE, Gardner C (1983) Spectroscopic measurement of hydrogen contamination in weld arc plasmas. J Appl Phys 54(9):4928–4938
14. Li JY, Song Y (1994) Spectral information of arc and welding automation. Weld World Lond 34:317
15. Mirapeix J, Cobo A, Conde O, Jaúregui C, López-Higuera J (2006) Real-time arc welding defect detection technique by means of plasma spectrum optical analysis. NDT & E Int 39(5):356–360
16. Yu H, Xu Y, Lv N, Chen H, Chen S (2013) Arc spectral processing technique with its application to wire feed monitoring in Al–Mg alloy pulsed gas tungsten arc welding. J Mater Process Technol 213(5):707–716
17. Zhang Z, Yu H, Lv N, Chen S (2013) Real-time defect detection in pulsed GTAW of Al alloys through on-line spectroscopy. J Mater Process Technol 213(7):1146–1156
18. Li PJ, Zhang YM (2000) Analysis of an arc light mechanism and its application in sensing of the GTAW process. Weld J N Y 79(9):252-s
19. Węglowski MS (2012) Monitoring of arc welding process based on arc light emission. INTECH Open Access Publisher
20. Guyon I, Elisseeff A (2003) An introduction to variable and feature selection. J Mach Learn Res 3:1157–1182
21. Frohlich H, Chapelle O, Scholkopf B (2003) Feature selection for support vector machines by means of genetic algorithm, Tools with Artificial Intelligence. Proceedings. 15th IEEE International Conference on, IEEE, pp 142–148
22. Foody GM, Mathur A (2004) Toward intelligent training of supervised image classifications: directing training data acquisition for SVM classification. Remote Sens Environ 93:107–117
23. Chang C-C, Lin C-J (2011) LIBSVM: A library for support vector machines. http://www.csie.ntu.edu.tw/cjlin/libsvm